Catalysis Science & Technology

An Enhanced Electrochemical CO2 Reduction Reaction on the SnOx-PdO surface of SnPd Nanoparticles Decorated on N-doped Carbon Fibers

Journal:	*Catalysis Science & Technology*
Manuscript ID	CY-ART-07-2020-001437.R1
Article Type:	Paper
Date Submitted by the Author:	02-Oct-2020
Complete List of Authors:	Narayanaru, Sreekanth; Tokyo Institute of Technology Institute of Innovative Research, Laboratory for Chemistry and Life Sciences Anilkumar, Gopinathan; Noritake Co., Limited, Research and Development Ito, Masaki; Noritake Co Ltd Research and Development Center Tamaki, Takanori; Tokyo Institute of Technology Institute of Innovative Research, Laboratory for Chemistry and Life Science, Institute of Innovative Research Yamaguchi, Takeo; Tokyo Institute of Technology Institute of Innovative Research, Laboratory for Chemistry and Life Science

ARTICLE

An Enhanced Electrochemical CO_2 Reduction Reaction on the SnOx-PdO surface of SnPd Nanoparticles Decorated on N-doped Carbon Fibers

Received 00th January 20xx,
Accepted 00th January 20xx

DOI: 10.1039/x0xx00000x

Sreekanth Narayanaru[a,b], Gopinathan M Anilkumar[a,b,c], Masaki ito[c], Takanori Tamaki[a,b], and Takeo Yamaguchi[a,b] *

In electrocatalytic CO_2 reduction reactions (CO_2RR), tin-based catalysts are known for their high formate faradaic yield. However higher overpotentials are required to attain a high faradaic yield with high partial current density for formate. Here, we describe the increase in the electrocatalytic CO_2RR activity of Sn nanoparticles decorated on nitrogen-doped carbon fibers (NCF) by adding a small amount of Pd. Nitrogen-doped carbon fibers decorated with SnPd nanoparticles ($Sn_{100-y}Pd_y$ –NCF) of different Sn: Pd ratios were synthesized using the electrospinning method and studied their electrocatalytic CO_2RR activity. The $Sn_{100-y}Pd_y$ –NCF catalyst with 3 wt.% (y= 3) of Pd displayed superior activity for CO_2RR and attained a faradaic efficiency of 85%, whereas the NCF with Sn nanoparticles (Sn_{100}–NCF) attained only 57% efficiency at the same potential. The surface electronic configuration, Tafel slope (79 mV/dec) and bicarbonate reduction activity of the catalyst reveal that the combination of SnO_x-PdO on the catalyst surface is responsible for the superior CO_2RR activity.

Introduction

Recent analyses have confirmed that the atmospheric CO_2 concentration reached 412 ppm, and its contribution to global warming is alarming [1-4]. In this context, reducing the global CO_2 emissions and converting CO_2 to useful products are the best solutions to control the CO_2-related climate change issues [5-8]. The electrochemical conversion of CO_2 to liquid fuels, such as formic acid/formate, methanol, and ethanol, or chemical feedstocks such as syngas, CO + H_2 [9-15] are the most promising methods for the effective utilization of CO_2. Recently, extensive investigations have been conducted across the world for the effective electrochemical reduction of CO_2. As a result, the electrocatalytic CO_2RR activity of a large number of materials was tested, which include metals [16-18], metal nanoparticles [19-23], bimetallic nanoparticles, metal nanoalloys [24-27], and many types of carbon materials [28-32]. These materials have different capabilities and product selectivity for CO_2RR. The product selectivity and efficiency vary with metals [18], the size of the metal particles [33], the roughness of the material surface [34, 35], the dopant in the carbon structure [28-30] and even the cations present in the electrolytes [35]. Therefore, tailor-made materials are important for the selective, efficient, and stable conversion of CO_2 to a product.

A variety of products have been produced from electrochemical CO_2RR [37]; however, techno-economic studies claim that CO_2 to formic acid/formate is one of the most economically viable products [38]. In the renewable energy industries, formic acid with a volumetric capacity of 53 g/L of hydrogen [39] and the liquid formate-based fuel cell (DFFC), which has the higher theoretical cell voltage (1.45 V) and low poisoning effect [40], confirms the importance of formic acid/formate as an energy carrier. Recently, researchers have focused on the development of highly efficient electrocatalysts and membranes for the formate oxidation reaction, which may facilitate the commercialization of direct formate fuel cells [41,42]. Even though DFFCs is considered as a source of green energy, the industrial production of formic acid/formate by the hydrolysis of methyl formate or formamide is not an eco-friendly method [43,44]. In this context, the efficient electrochemical reduction of CO_2 to formate using renewable energy sources is a promising method for utilizing CO_2 and producing clean and sustainable fuels.

Among the metal catalysts, the Sn-based catalysts have an efficient electrochemical CO_2 reduction activity. Tin has a high hydrogen overpotential and excellent selectivity for CO_2 to formate conversion [19,45-50]; tin is also a non-toxic, inexpensive, and eco-friendly element. Furthermore, the native oxide layer of the Sn surface increases the catalytic activity by stabilizing the CO_2 radical ($CO_2^{\bullet-}$) [50]. Although tin displays a high selectivity and efficiency for the CO_2 reduction reaction (CO_2RR), the requirement of high overpotential is the main drawback. A variety of modifications have been introduced to reduce the overpotential and improve the catalytic activity of Sn [19,45-49], but the ability to achieve high faradaic efficiency and a high partial current density remains a substantial

[a] Laboratory for Chemistry and Life Sciences, Tokyo Institute of Technology, R1-17, 4259 Nagatsuta, Midori-Ku, Yokohama, Japan 226-8503. E-mail: yamag@res.titech.ac.jp
[b] Core Research for Evolutionary Science and Technology, Japan Science and Technology Agency (JST-CREST), Japan 102-0076.
[c] R&D Center, Noritake Co., Ltd., 300 Higashiyama, Miyochi-cho, Miyoshi, Japan 470-0293.

†Electronic Supplementary Information (ESI) available: [details of any supplementary information available should be included here]. See DOI: 10.1039/x0xx00000x

challenge. In the present study, we prepared Sn nanoparticles with a low amount of Pd that were supported on N-doped carbon fibers (NCFs) using a simple electrospinning method and investigated the electrocatalytic CO_2 reduction activity of these materials. Compared to the usual carbon support for nanoparticles, N-doped carbon surface is more suitable since pyridinic nitrogen in N-doped CNFs possesses catalytic CO_2 reduction reaction activity [28,29]. We chose palladium as an additive to tin to increase the CO_2RR activity because the Pd surface is capable of stabilizing and reducing bicarbonate ions to formate at a near thermodynamic potential [51,52]. Since the bicarbonate ions are the proton source for the CO_2 reduction reaction in bicarbonate solution [19,21], the catalyst surface stabilized bicarbonate ions may enhance the quick protonation of $CO_2^{\bullet-}$. Based on this information, we prepared $Sn_{100-y}Pd_y$ –NCF catalysts with different amounts of Pd loading. As a result of this rational design of the electrocatalyst, we obtained a maximum faradaic efficiency of 85% and a partial current density of 12.75 mA cm^{-2} during the electrochemical reduction of CO_2 on the $Sn_{100-y}Pd_y$–NCF catalyst with 3 wt.% (y=3) Pd. The material characterization and analysis of the electrochemical activity of these catalysts confirm that the combination of SnO_x-PdO (where SnO_x is the sum of the SnO and SnO_2) on the catalyst surface is responsible for this superior activity.

2.Experimental

2.1. Chemicals

N-doped carbon fibers with Sn and Pd nanoparticles were prepared using $SnCl_2.2H_2O$ (Wako Chemicals), Pd $(CH_3COO)_2$ (Sigma-Aldrich), Polyacrylonitrile (PAN, MW= 150,000) (Sigma-Aldrich), and DMF (Wako Chemicals) as precursors. Electrolytes were prepared using $KHCO_3$ (Wako Chemicals), H_2SO_4 (Wako Chemicals), potassium formate (Wako Chemicals), disodium hydrogen phosphate, and monosodium hydrogen formate (Wako Chemicals). DMSO (Sigma-Aldrich) and D_2O (Wako Chemicals) were used for NMR analyses. All solutions were prepared in Milli-Q water (18.2 MΩ).

2.2. Synthesis and characterization of metal nanoparticles decorated on N-doped carbon fibers

Tin nanoparticles decorated on N-doped carbon fibers (Sn_{100}–NCF) were prepared by an electrospinning method using a NANON-01A (MECC Co., Ltd.) electrospinning system. A solution containing 1.2 g of polyacrylonitrile (PAN), 1 g of $SnCl_2.2H_2O$ and 12.8 g of DMF was electrospun to produce Sn_{100}–NCF. The following electrospinning conditions were applied, applied voltage of 25 kV, a distance of 150 mm was maintained between the needle and collector, and precursor solution fed with a feed rate of 0.8 mL/hour. After electrospinning, fibers were dried at 130°C for 12 hours in a vacuum atmosphere, and the dried fibers were heated at 280°C for 90 minutes in an air atmosphere at a heating rate of 5°C/minute to stabilize the PAN fibers. The stabilized composite PAN fibers were then heated at 900°C for 120 minutes at a ramping rate of 3°C/minutes under N_2/H_2 (100 sccm N_2 and 30 sccm H_2) atmosphere. Various $Sn_{100-y}Pd_y$–NCF catalyst samples with different amounts of Pd were prepared using the method described above. For $Sn_{100-y}Pd_y$ –NCFs the solution for electrospinning was prepared by adding the required amount of metal precursors to PAN (1.2 g) in a DMF (9.8 g) solution. Metal precursor solutions were prepared by separately dissolving Pd $(Ac)_2$ (25, 50, 75, and 100 mg) and $SnCl_2.2H_2O$ (1 g) in 1.5 mL of DMF, and then the two solutions were mixed and sonicated for 30 minutes.

The ICP analysis was performed using a Shimadzu sequential plasma emission spectrometer ICP2-8100 to quantify the total metal loading and the weight percentage distribution of Sn and Pd on NCF (details are provided in the ESI, Table S1). Phase identification and crystallinity of the catalyst samples were determined by performing XRD analysis at a scan rate of 1°/minute using an Ultima IV system from Rigaku with a Cu Kα (λ= 1.5406 Å) and X-ray source operating at 40 kV and 40 mA. The surface compositions of the fibers were analyzed using XPS Quantum 2000, ULVAC–PHI Inc., with a twin-anode X-ray source using Al Kα radiation (hυ = 1486.58 eV). FESEM (S-4800, Hitachi High Technology) operating at an acceleration voltage of 5 kV and HR-TEM (TOPCON EM – 002BF – J) operating at an acceleration voltage of 200 kV with a twin EDS facility was used to visualize the morphology and to understand the elemental distribution of nanoparticle-decorated fibers.

2.3. Electrochemical Characterization

The electrochemical activity of the catalysts was studied using an electrochemical measurement system (Hokuto Denko, HZ5000). Linear sweep voltammetry (LSV), cyclic voltammetry (CV) and constant potential electrolysis were performed in a two-compartment cell separated by a Nafion-117 membrane. An Ag/AgCl (KCl-saturated) reference electrode was used for all measurements, and Pt foil (area: 18 cm^2) served as the counter electrode. Catalyst ink was prepared by mixing the required amount of catalyst in a solution containing 5 mL of isopropanol (25 wt.%) and 20 µL of the Nafion® solution (5 wt.%). The catalyst ink was sonicated for 4 hours in an ice bath to obtain a good dispersion. After achieving a well-dispersed solution, the catalyst was coated on the glassy carbon electrode using the drop-casting method, and the catalyst loading was maintained at 50 µg of metal/cm^2 for all the samples. The catalyst-coated glassy carbon electrode (Hokuto Denko) with an electrode area of 0.196 cm^2 was used for voltammetric and impedance analyses. The catalyst-coated, 1 cm^2 Sigracet 28 BA gas diffusion layer (GDL) electrode was used for electrolysis and stability studies. For CO_2RR, a 0.5 M $KHCO_3$ solution was first saturated with CO_2 by bubbling it with CO_2 gas for 1 h. During electrolysis, a constant flow of CO_2 gas was maintained at the cathode compartment. Similarly, the bicarbonate reduction reaction was performed by passing N_2 instead of CO_2 in a 0.5 M $KHCO_3$ solution. All applied potential values reported here are iR corrected and with respect to a reversible hydrogen electrode (RHE). The conversion of the applied potential measured using the Ag/AgCl electrode to the RHE was calculated using a method described in the ESI (Section S4).

2.4. Product analysis

Liquid product quantification was performed using a Bruker 400 MHz NMR spectrometer with DMSO as the internal standard. The details of the analysis and quantification of the liquid products using NMR are provided in the ESI (Section S6.1).

Gas products were quantified using a gas chromatograph (Shimadzu GC-2010 Tracera) equipped with Micropacked ST in series with Shincarbon ST column and Barrier Discharge Ionization Detector (BID). The details of the analysis and quantification of the gas products using gas chromatography are provided in the ESI (S6.2).

3. Results and discussion

3.1. Synthesis and Characterization of the catalyst.

In the stabilization process of the as-spun fibers at 280°C in air, polyacrylonitrile undergoes crosslinking to form a stable fibrous structure [53]. Pyrolysis at 900°C under the N_2/H_2 atmosphere after stabilizing the fibers with metal precursors produce metal nanoparticles-decorated graphitized N-doped carbon fibers. Based on the amount (wt.%) of Sn and Pd present in the NCF, the catalyst samples are designated as Sn_{100}–NCF, $Sn_{97}Pd_3$–NCF, $Sn_{95}Pd_5$–NCF, $Sn_{94}Pd_6$–NCF, and $Sn_{91}Pd_9$–NCF, here the numbers represent the percentage of Sn and Pd in the total metal loaded on the NCF in all other cases.

X-ray diffraction (XRD) patterns of all the samples are presented in Figure 1a. The XRD pattern of the Sn_{100}–NCF sample indicated that the metallic tin was a major phase, along with a small amount of SnO_2. The diffraction patterns correspond to 2θ values of 30.67, 32.06, 43.92, and 44.98 representing the metallic tin (200), (101), (220) and (211) planes, respectively (JCPDS No: 83-7910), and 2θ values of 26.61, 33.89 and 51.79 correspond to the SnO_2 (110), (101), and (211) planes, respectively, (JCPDS No: 41-1445). The XRD patterns of $Sn_{97}Pd_3$–NCF and $Sn_{95}Pd_5$–NCF also showed the presence of Sn and SnO_2, similar to the Sn_{100}-NCF sample. In addition to Sn and SnO_2, the presence of PdO was also observed at 2θ values of 34.8 and 42.4, representing the PdO (101) and (110) planes, respectively (JCPDS No 43-1024). The catalysts with comparatively high Pd concentration, $Sn_{94}Pd_6$–NCF and $Sn_{91}Pd_9$–NCF the XRD peaks corresponding to SnO_2 and PdO was not observed; however, a slight shift in the diffraction peaks of Sn to higher 2 theta values, 0.05 and 0.13 degrees, respectively was noticed (Figure 1b) compared to Sn_{100}–NCF, $Sn_{97}Pd_3$–NCF and $Sn_{95}Pd_5$–NCF, indicating the possible formation of an SnPd alloy [54]. Although the total amount of Pd present in $Sn_{97}Pd_3$–NCF and $Sn_{95}Pd_5$–NCF is low, the appearance of the PdO peak indicated that most of the Pd is located on the surface and exists as PdO.

XPS analysis of the catalysts was performed to identify the surface composition (Figures 1c-e, S1, and S2). The deconvoluted high-resolution XPS N-1s spectra of all catalyst samples indicated the presence of graphitic (BE = 400.76 eV), pyrrolic (BE =399.60 eV), and pyridinic (BE=398.30 eV) nitrogen [32]. The deconvoluted Sn-3d spectra of all catalysts showed the presence of Sn, SnO, and SnO_2. The binding energy values of Sn ($3d_{5/2}$ – 485.1 eV), SnO ($3d_{5/2}$ – 486.2 eV), and SnO_2 ($3d_{5/2}$ – 487.2 eV) [55] were approximately the same for all catalysts, with a negligible difference. The atomic percentages (at.%) of Sn, SnO, and SnO_2 were calculated from the corresponding peak area of the deconvoluted Sn-$3d_{5/2}$ spectrum (Table S2a). For all catalysts, the amount (at.%) of SnO_x was greater than 95%, suggesting that the catalyst surface consists of an oxide layer of Sn. The deconvoluted Pd-3d spectrum was different for different $Sn_{100-y}Pd_y$–NCF samples (Figures 1e and S2); the spectrum of $Sn_{97}Pd_3$–NCF contained only the PdO peak ($3d_{5/2}$ – 336.9 eV), but peaks for both PdO and Pd ($3d_{5/2}$ – 335.5 eV) were observed in the spectrum of $Sn_{95}Pd_5$–NCF. For $Sn_{94}Pd_6$–NCF and $Sn_{91}Pd_9$–NCF samples, both Pd and PdO peaks were slightly shifted to higher binding energy [57]. Pd and PdO peaks of $Sn_{94}Pd_6$ – NCF were observed at $3d_{5/2}$ – 336.2 eV and $3d_{5/2}$ – 337.3 eV, respectively, and at $3d_{5/2}$ – 336.4 eV and 337.5 eV for $Sn_{91}Pd_9$–NCF, indicating a change in the binding energy values of Pd and PdO probably due to the formation of SnPd alloy [57, 58]. The ratio of Pd/PdO of the $Sn_{100-y}Pd_y$–NCF systems increased with the increase in the Pd concentration (Table S2b). The XRD and XPS analyses revealed that the core of metal nanoparticles in Sn_{100}-NCF and $Sn_{100-y}Pd_y$–NCF consisted of metallic Sn and the surface in the oxidized form. The surface of $Sn_{97}Pd_3$–NCF solely consists of SnO_x and

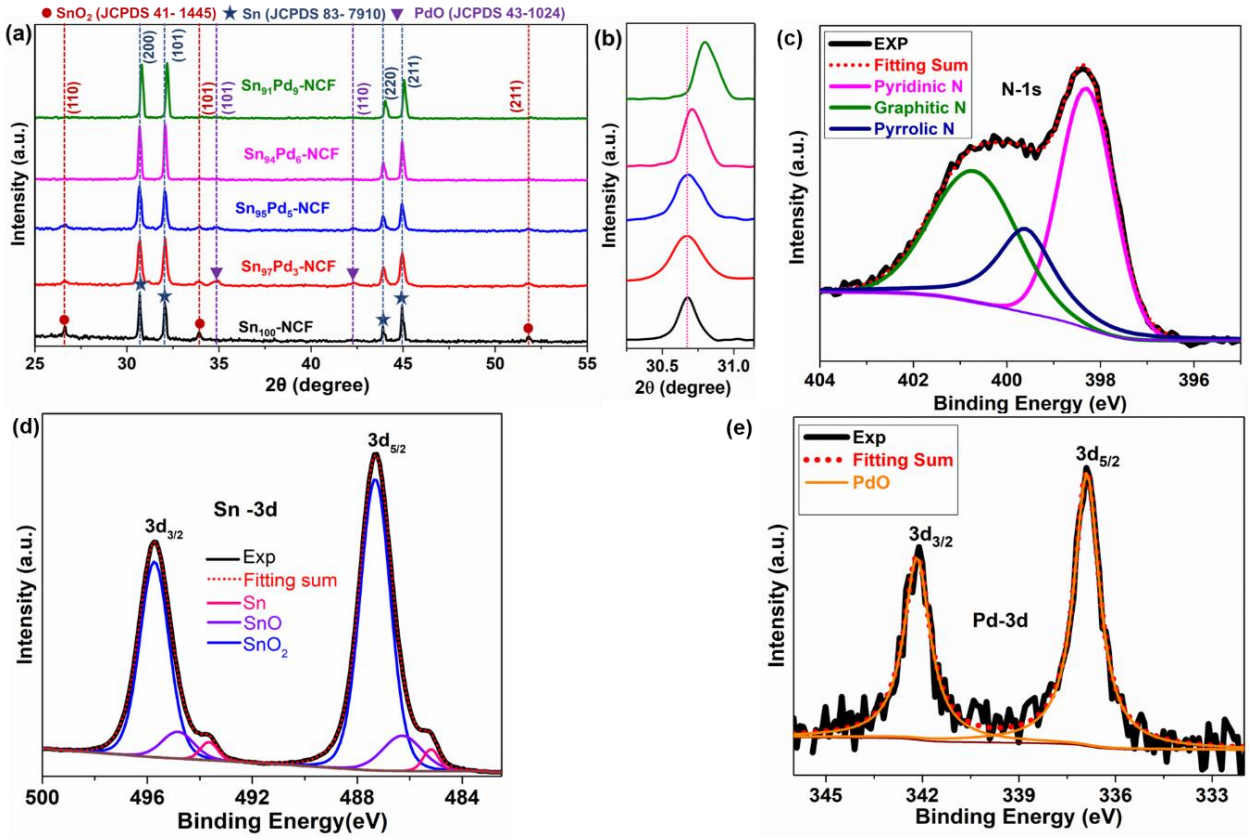

Figure 1. XRD patterns of (a) Sn_{100}-NCF and $Sn_{100-y}Pd_y$–NCF catalysts, (b) highlighted, 2θ values between 30 to 31 degree, and (c-e) the deconvoluted XPS spectra of N, Sn and Pd present in $Sn_{97}Pd_3$- NCF.

PdO, whereas the surface of the $Sn_{95}Pd_5$–NCF system is mainly composed of SnO_x, PdO, and a low amount of Pd. For the $Sn_{94}Pd_6$–NCF and $Sn_{91}Pd_9$–NCF samples, the surface concentration of Pd is higher than the PdO concentration. In general, the XPS results corroborate the XRD results

The morphology of the materials was analyzed using FE-SEM and HR-TEM. The average diameter of N-doped carbon fibers was 650 nm (Figure 2a), and the nanoparticles were spherical with a size of less than 10 nm uniformly decorated the carbon fibers (Figure 2 b and c). Lattice fringes with a d-spacing of 0.29 nm (inset of Figure 2d), corresponds to the (200) plane of Sn (JCPDS No: 83-7910). The energy-dispersive X-ray spectroscopy (EDS) map revealed the uniform distribution of C, N, O, Sn, and Pd on the $Sn_{100-y}Pd_y$–NCF surface (Figures 2 f-j and S3).

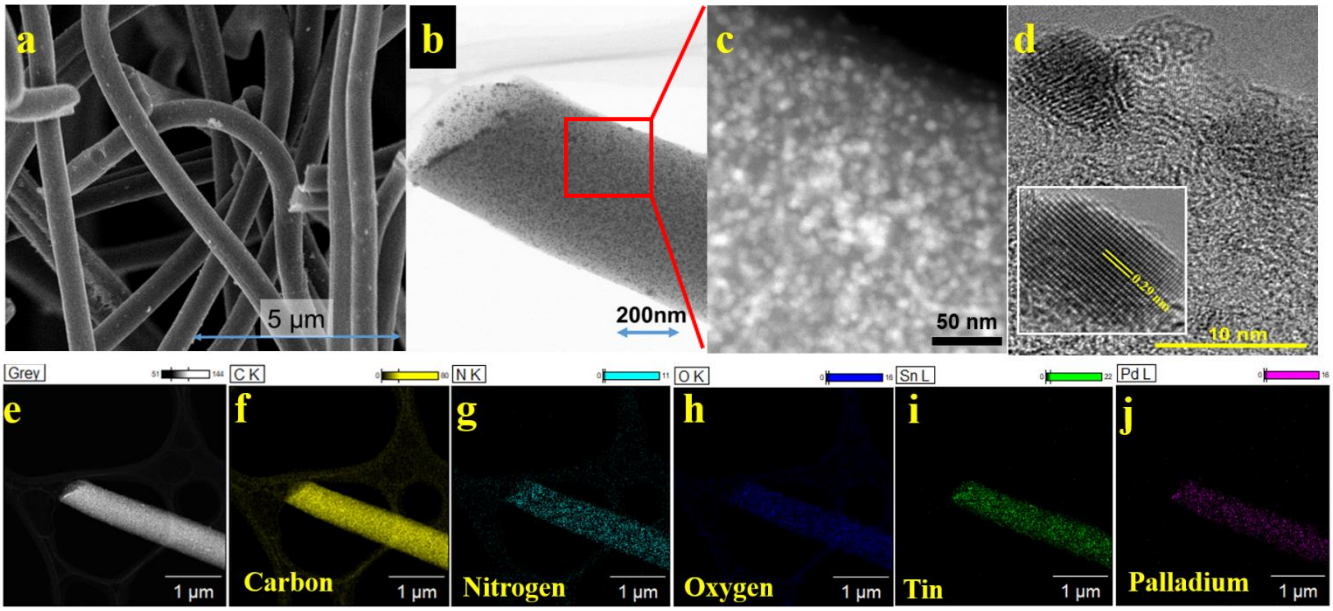

Figure 2. (a) General morphology of $Sn_{97}Pd_3$–NCF (SEM image). HR-TEM images of (b) a single fiber of $Sn_{97}Pd_3$–NCF and (c) SnPd nanoparticles dispersed on the carbon fiber (d) showing the lattice fringes corresponding to the Sn (200) plane. (f-j) STEM-EDS mapping images of C, N, O, Sn and Pd, respectively.

3.2. Electrochemical Reduction of CO_2

The electrocatalytic CO_2 reduction activity of all materials was primarily evaluated using linear sweep voltammetry (LSV). Figures 3a and S5 show the voltammograms of Sn_{100}–NCF, $Sn_{100-y}Pd_y$–NCF, and NCF, recorded between –0.1 V and –1 V at a scan rate of 10 mV s^{-1} in CO_2 saturated 0.5 M $KHCO_3$. Based on the previous reports, that the potential at which the catalyst attains a current density value of –0.15 mA/cm^2 is considered as the onset potential[29].The onset potential values of NCF, Sn_{100}–NCF, $Sn_{91}Pd_9$–NCF, $Sn_{94}Pd_6$–NCF, $Sn_{95}Pd_5$–NCF, and $Sn_{97}Pd_3$–NCF were – 0.36, – 0.21, – 0.17, – 0.16, – 0.14 and – 0.12 V respectively. At – 1.0 V the NCF alone attained a current density value of 0.77 mA cm^{-2}, whereas the Sn_{100}–NCF catalyst attained a current density value of 8.23 mA cm^{-2} at the same potential. $Sn_{97}Pd_3$–NCF, $Sn_{95}Pd_5$–NCF, $Sn_{94}Pd_6$–NCF, and $Sn_{91}Pd_9$–NCF attained a current density value of 19.75, 18.88, 14.12, and 12.07 mA cm^{-2} respectively at –1.0 V. However, the current density alone not ensure the CO_2RR activity of the catalysts. So the product analysis was performed after 30 minutes of electrolysis at different potentials and calculated the faradaic efficiency of each product. The liquid and gaseous products of CO_2RR were qualitatively and quantitatively analyzed using NMR and gas chromatography respectively. For all the catalysts, formate was the initial CO_2RR product obtained. Formate production was observed for $Sn_{100-y}Pd_y$–NCF samples at –0.37 V, whereas for Sn_{100}–NCF and NCF, the potential was –0.57 V, which is 0.2 V higher than the $Sn_{100-y}Pd_y$–NCF catalysts. N-doped carbon can produce CO and formate from CO_2 [28,29], however in this work NCF produced only formate. For all other catalysts, the products of CO_2RR were formate and CO, of which formate was the major product. The faradaic efficiency (FE_{CO2RR}) and partial current density (j_{CO2RR}) of CO_2RR products of all the samples were measured and the results are presented in Figures 3b, 3c, S8 - S10 and Table 1. The NCF attained a FE_{CO2RR} of 56 % and j_{CO2RR} 0.41 mA cm^{-2} at –0.97 V, whereas at the same potential Sn_{100}–NCF attained a faradaic efficiency of 65% for CO_2RR at –0.97 V with j_{CO2RR} of 4.60 mA cm^{-2}, the formate faradaic efficiency ($FE_{formate}$) was 57% and the corresponding partial current density of formate ($j_{formate}$) was 4.03 mA cm^{-2}.

The $Sn_{100-y}Pd_y$–NCF catalysts have displayed an interesting trend in FE_{CO2RR}. $Sn_{94}Pd_6$–NCF and $Sn_{91}Pd_9$–NCF catalysts exhibited a high FE_{CO2RR} at low overpotential region compared to $Sn_{97}Pd_3$–NCF and $Sn_{95}Pd_5$–NCF. However, at slightly higher overpotential, $Sn_{97}Pd_3$–NCF and $Sn_{95}Pd_5$–NCF attained very high FE_{CO2RR} and j_{CO2RR} values compared to the other two $Sn_{100-y}Pd_y$–NCF catalysts. The faradaic efficiency values of formate and CO of $Sn_{100-y}Pd_y$–NCFs revealed that formate is the major CO_2RR products for all the catalysts. Among the $Sn_{100-y}Pd_y$–NCF catalysts the $Sn_{97}Pd_3$–NCF has attained high $FE_{formate}$ and $j_{formate}$ values, when evaluating the catalysts in terms of the faradaic efficiency of CO (FE_{CO}), the $Sn_{91}Pd_9$–NCF has attained high $FE_{CO,\ 30\%\ at}$ – 0.77 V (Figure 3c). Comparing the activity of efficient $Sn_{100-y}Pd_y$–NCF catalysts with Sn_{100}–NCF in terms $FE_{formate}$, the highly efficient $Sn_{97}Pd_3$–NCF has a 27% higher $FE_{formate}$ and 8 mAcm^{-2} *higher* $j_{formate}$ than Sn_{100}–NCF at –0.92 V (Figure 3b and S9b). Similarly, comparing the activity in terms of FE_{CO}, the $Sn_{91}Pd_9$–NCF exhibited a 26% higher FE_{CO} and 0.96 mAcm^{-2} j_{CO} than Sn_{100}–NCF at –0.77 V (Figure 3c, S9c). These results suggest that a small amount of Pd addition on Sn –NCF, either as Pd or PdO can enhance the CO_2RR

activity. Based on the material characterization, and faradaic efficiency of formate and CO results of the most efficient $Sn_{100-y}Pd_y$–NCF catalysts we can say that SnOx–Pd enhances CO production and SnOx–PdO enhances formate production. The CO_2RR activity of pure Pd is well studied and reported that at low overpotentials Pd produces formate and CO and at higher overpotentials, Pd preferably produces CO [59, 60], but the activity of PdO is not well understood. We performed CO_2 reduction over PdO surface (Section S8, Figure S11a). During the initial stages of electrolysis, the FE formate reached 64% but it quickly reduced and stabilized at 34%, the $j_{formate}$ was <1 $mAcm^{-2}$. The XRD analysis at different stages of electrolysis confirm that PdO reduced Pd during the electrolysis (Figure S11b).

Since PdO was quickly reducing to Pd during the electrolysis, we tested the catalytic stability of $Sn_{97}Pd_3$ –NCF (Figure S12) with periodic analysis of Faradaic efficiency, followed by XPS and HR-TEM of the catalyst (Figure S13). Interestingly a stable FE_{CO2RR} was retained for $Sn_{97}Pd_3$ –NCF for up to 9 hours of electrolysis, and then a decrease in FE_{CO2RR} was observed. After 15 hours, the FE_{CO2RR} decreased to 70% from 85%. $FE_{formate}$ and FE_{CO} were 68% and 2%, respectively. XPS analysis was performed after 9 and 15 hours of electrolysis. After 9 hours of electrolysis the PdO at% was only reduced to 60 from 100%, the at% of SnO_x remained almost the same,96.4 from 96.7, (Figure S13 a and b). The XPS analysis after 15 hours of electrolysis, the

Table 1. The potential at which the maximum FE_{CO2RR} obtained, corresponding FE_{CO2RR}, $FE_{formate}$, FE_{CO}, FE_{H2}, j_{CO2RR} and $j_{formate}$, of the catalysts

Catalyst	E at maximum FE_{CO2RR} (V)	FE_{CO2RR} (%)	$FE_{formate}$ (%)	FE_{CO} (%)	FE_{H2} (%)	j_{CO2RR} (mA cm^{-2})	$j_{formate}$ (mA cm^{-2})	j_{CO} (mA cm^{-2})	j_{H2} (mA cm^{-2})
$Sn_{91}Pd_9$–NCF	–0.87	67	58	9	33	3.79	3.28	0.51	1.87
$Sn_{94}Pd_6$–NCF	–0.87	70	60	10	30	4.20	3.60	0.60	1.80
$Sn_{95}Pd_5$–NCF	– 0.92	81	70	11	19	10.84	9.36	1.48	2.54
$Sn_{97}Pd_3$–NCF	– 0.92	85	77	8	15	12.75	11.55	1.20	2.25
Sn_{100}–NCF	– 0.97	65	57	8	35	4.60	4.03	0.57	2.4
NCF	–0.97	56	56	0	44	0.41	0.41	-	0.32

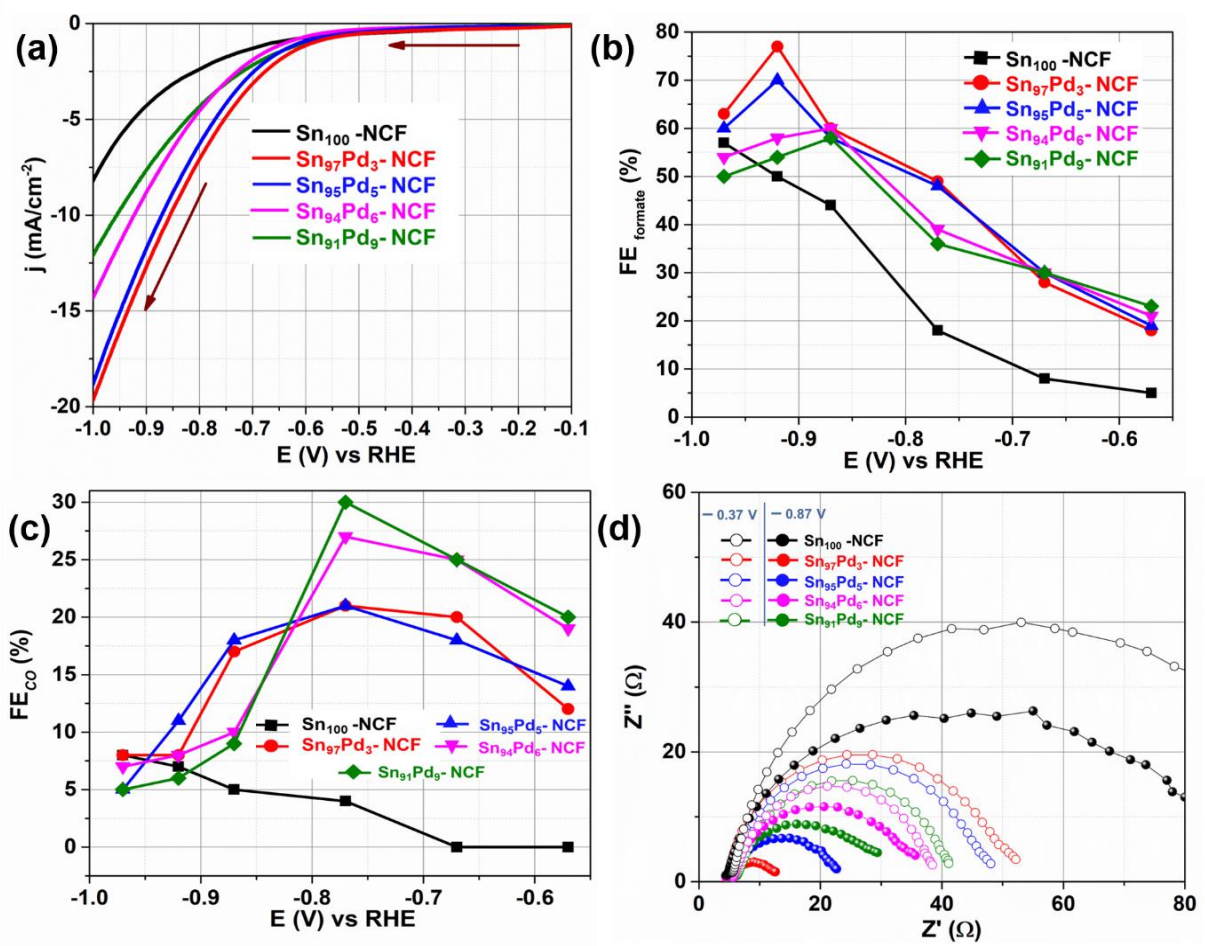

Figure 3. Electrocatalytic CO_2 reduction in 0.5 M $KHCO_3$ saturated with CO_2 on Sn_{100}–NCF and $Sn_{100-y}Pd_y$–NCF catalysts. (a) iR-corrected linear sweep voltammogram measured at a scan rate of 10 mV/s, (b) Formate faradaic efficiency, (c) CO faradaic efficiency and (d) Nyquist plots measured at –0.37 V and –0.87 V.

atomic percentage of Sn at the surface was increased from 3.26 to 18 and the atomic percentage of SnOx reduced to 82 from 96.74 (Figure S13 c). A very low-intensity broad Pd -3d peak was obtained. The TEM image of the catalyst, after 15 hours of electrolysis shows agglomeration of the particles on the surface (Figure S13 d), whereas the particles inside the fibers have not changed. The stability test and followed material characterization confirms that the PdO reduction is slower in the $Sn_{97}Pd_3$ –NCF and the FE_{CO2RR} reduces with the reduction in PdO.

Impedance and Tafel slope analysis were performed to understand the charge transfer kinetics and the reaction mechanism. The electrochemical impedance was measured at a lower overpotential, –0.37 V, and a higher overpotential, –0.87 V in a CO_2-saturated $KHCO_3$ solution. At –0.37 V, $Sn_{91}Pd_9$–NCF and $Sn_{94}Pd_6$–NCF displayed a low charge transfer resistant (R_{CT}) than $Sn_{97}Pd_3$–NCF and $Sn_{95}Pd_5$–NCF. The trend changed when the R_{CT} value was measured at –0.87 V, the $Sn_{97}Pd_3$–NCF, and $Sn_{95}Pd_5$–NCF samples displayed a lower R_{CT} value than the $Sn_{91}Pd_9$–NCF and $Sn_{94}Pd_6$–NCF catalysts (Figure 3d and Table S3). Furthermore, we performed the EIS analysis before and after 30 minutes of electrolysis for the $Sn_{97}Pd_3$–NCF and $Sn_{91}Pd_9$–NCF catalysts (Figure S14). The R_{CT} values of $Sn_{91}Pd_9$–NCF increased with the time of electrolysis, whereas the change in R_{CT} values was not significant for $Sn_{97}Pd_3$–NCF. The increase in the R_{CT} values of $Sn_{91}Pd_9$–NCF with the time of electrolysis is probably because of the adsorption of intermediates or products on the catalytic surface and hinder the electron transfer. To verify this possibility the $Sn_{91}Pd_9$–NCF electrode was kept at 0.5 V for 30 s after electrolysis and then EIS was measured; the R_{CT} was similar to the initial R_{CT}, suggesting the adsorption of an intermediate or reaction products on the catalyst surface. Since the Pd surface is susceptible to CO poisoning [59 -61], the increased R_{CT} values with respect to time of electrolysis are possibly due to CO poisoning. The low or insignificant change in the R_{CT} values of $Sn_{97}Pd_3$–NCF after electrolysis revealed that the PdO surface is not susceptible to CO poisoning [62]. The increase in R_{CT} values of $Sn_{91}Pd_9$–NCF and $Sn_{94}Pd_6$–NCF at high overpotentials is due to surface poisoning and these results corroborate their low current density and faradaic efficiency at higher overpotentials.

Tafel slopes (Figures 4 and S15) were plotted using the log of $j_{formate}$ and overpotentials of each sample to understand the reaction mechanism. Tafel slope values for Sn_{100}–NCF, $Sn_{97}Pd_3$–NCF, $Sn_{95}Pd_5$–NCF, $Sn_{94}Pd_6$–NCF, and $Sn_{91}Pd_9$–NCF were 105, 79, 92, 105 and 117 mv/dec, respectively. Tafel slope value of $Sn_{97}Pd_3$–NCF and $Sn_{95}Pd_5$–NCF was less than 120 mv/dec and close to 59 mv/dec. The low Tafel slope value says that the first step of the reaction mechanism was a reversible one-electron transfer to CO_2 to form $CO_2^{\bullet-}$ then the chemical rate-determining step, i.e. the protonation of C in $CO_2^{\bullet-}$ to form formate [19, 48,49]. Higher Tafel slope values closer to 120 mv/dec suggest that the one-electron transfer to CO_2 to form $CO_2^{\bullet-}$ is the rate-limiting step [19,42,45]. According to previous reports, the surface electronic structure plays a major role in the selectivity of CO_2 reduction reactions by stabilizing $CO_2^{\bullet-}$ and other intermediates [21,33,34,48]. Here, the low Tafel slope, high faradaic efficiency, and partial current density obtained for $Sn_{97}Pd_3$–NCF and $Sn_{95}Pd_5$–NCF confirm that the presence of SnO_x-PdO combination at the catalyst surface has an important role in their catalytic activity. A recent study by Zhang et al., on the electrochemical reduction of CO_2 using a Pd/SnO_2 system explained the role of the Pd–O–Sn combination in promoting the reaction through excellent CO_2 adsorption and decreasing CO poisoning on the Pd surface [62].

In the electrochemical CO_2 reduction reaction, bicarbonate ions in the electrolyte provide protons to protonate $CO_2^{\bullet-}$ and produce

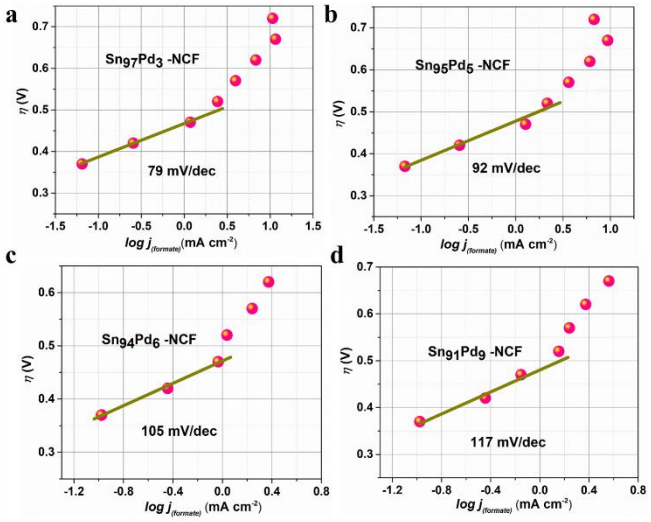

Figure 4. Tafel slopes of (a) $Sn_{97}Pd_3$–NCF (b) $Sn_{95}Pd_5$–NCF (c) $Sn_{94}Pd_6$–NCF and (d) $Sn_{91}Pd_9$–NCF.

formate [19,21]. A catalyst surface, which can stabilize the bicarbonate ions on its surface, can facilitate the quick protonation of $CO_2^{\bullet-}$ to formate. We believe that the reason for high current density and the Faradaic efficiency of SnPd –NCF catalyst with the SnO_x-PdO surface is because the SnO_x-PdO surface effectively stabilizes $CO_2^{\bullet-}$ and bicarbonate on its surface and protonates $CO_2^{\bullet-}$ to produce formate. To ensure this possibility, we tested the bicarbonate reduction activity of all catalysts and analyzed the products. The NCF and Sn_{100}–NCF catalysts were unable to reduce bicarbonate to formate whereas, formate was produced when we performed bicarbonate reduction over $Sn_{100-y}Pd_y$–NCF. Only a detectable amount of formate ($FE_{formate}$ < 1%) was obtained from $Sn_{91}Pd_9$–NCF and $Sn_{94}Pd_6$–NCF. However, a quantifiable amount of formate ($FE_{formate}$> 3%) was obtained from the catalysts $Sn_{95}Pd_5$–NCF and $Sn_{97}Pd_3$–NCF (Figure S16). A low amount of formate formation suggests that the bicarbonate reduction is not kinetically feasible on the SnO_x-PdO surface, but the electrode stabilizes the bicarbonate ions on its surface. Compiling the results obtained from the material characterizations, electrochemical CO_2RR, and bicarbonate reduction reaction, the catalyst surface with the SnO_x-PdO combination appeared to be more active than a catalyst surface with SnO_x and SnO_x-Pd. Further, we investigated the bicarbonate reduction activity of Pd and PdO by conducting bicarbonate electrolysis on bare Pd and oxidized Pd electrode. The bicarbonate electrolysis performed on the Pd surface produced no formate, however, formate was obtained when the electrolysis was performed on PdO (Section S-14 and Figure S-17), revealing that PdO surface is capable to stabilize and reduce bicarbonate ion.

Based on these analyses and previously reported mechanisms [19,62,63], we speculate the probable CO_2 reduction reaction mechanism on Sn_{100}–NCF with SnOx (scheme 1) and SnPd–NCF with SnOx-PdO (scheme 2) as described below, however detailed in-situ studies are warranted to confirm this mechanism. The CO_2 reduction mechanism on the Sn_{100}–NCF catalyst involves the formation and stabilization of $CO_2^{\bullet-}$ at the catalyst surface. Stabilized $CO_2^{\bullet-}$ further accepts a proton from the bicarbonate ions of the electrolyte to form formate (scheme -1) [19,63]. However, on the $Sn_{100-y}Pd_y$–NCF surface with SnO_x-PdO, the bicarbonate ion adsorbed on the catalyst surface protonates $CO_2^{\bullet-}$ to produce formate (Scheme -2).

Scheme 1. CO_2 reduction to formate on the Sn_{100}–NCF surface

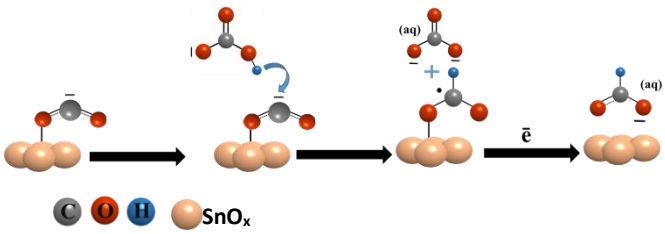

Scheme 2. CO_2 reduction to formate on the SnOx-PdO surface

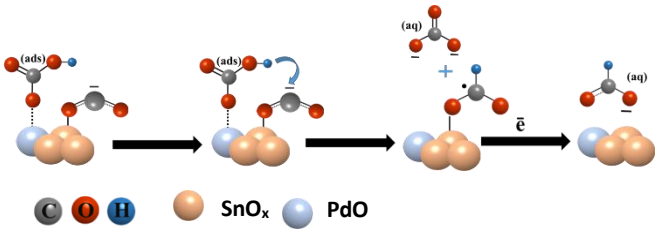

4. Conclusions

In conclusion, the electrocatalytic CO_2 reduction reaction activity of SnPd nanoparticles decorated on N-doped carbon fibers with different Pd contents was analyzed. The catalysts were prepared using a simple one-step electrospinning method followed by pyrolysis. The $Sn_{100-y}Pd_y$–NCF catalyst with a low Pd content, 3 wt.% Pd, showed superior CO_2RR activity (total Faradaic efficiency of 85% and a partial current density of 12.7 mA.cm^{-2} at –0.92 V compared with RHE) to the $Sn_{100-y}Pd_y$–NCF catalysts with a high Pd content. The analysis of the surface composition revealed that $Sn_{100-y}Pd_y$–NCF with 3 wt.% Pd mainly contained PdO and SnOx on its surface. The Tafel slope analysis and bicarbonate reduction activity of $Sn_{97}Pd_3$–NCF catalysts suggest a possibility that the SnO_x–PdO species at the catalyst surface effectively stabilize $CO_2^{\bullet-}$ and bicarbonate on its surface. Simultaneous stabilization of bicarbonate anions and $CO_2^{\bullet-}$ on the catalytic surface can promote the CO_2RR by quick protonation of $CO_2^{\bullet-}$ to produce formate.

Conflicts of interest

There are no conflicts to declare

Acknowledgements

The authors acknowledge the financial assistance from the Japan Science and Technology (JST) Core Research for Evolutionary Science and Technology, Japan Science and Technology Agency (JST-CREST, JPMJCR 1543), and this study was also supported in part by the "Five-Star Alliance". Professor Ken Motokura, Tokyo Institute of Technology, is gratefully acknowledged for providing access to the gas chromatography facility.

Notes and references

1 Earth System Research Laboratory Global Monitoring Division, Mauna Loa observatory. https://www.esrl.noaa.gov/gmd/webdata/ccgg/trends/co2_data_mlo.png
2 T. R. Karl and K. E. Trenberth, Science, 2003, 302, 1719-1723.
3 S. H. Schneider, Science .1989, 243, 771-781.
4 D. Tong, Q. Zhang, Y. Zheng, K. Caldeira, C. Shearer, C. Hong, Y. Qin and S. J. Davis, Nature, 2019,572, 373–377.
5 C. Song, Catal. Today, 2006, 115, 2-32.
6 E. Alper and O. Yuksel Orhan, Petroleum, 2017, 3, 109-126.
7 C. Ampelli, S. Perathoner, and G. Centi, Philos. Trans. R. Soc. A Math. Phys. Eng. Sci., 2015, 373, 1-30.
8 M. Mikkelsen, M. Jørgensen and F. C. Krebs, Energy Environ. Sci., 2010, 3, 43–81.
9 E. E. Benson, C. P. Kubiak, A. J. Sathrum and J. M. Smieja, Chem. Soc. Rev., 2009, 38, 89–99.
10 S. Back, H. Kim, and Y. Jung, ACS Catal., 2015, 5, 965–971.
11 G. Centi, C. Ampelli, C. Genovese, B. C. Marepally, G. Papanikolaou, and S. Perathoner, Faraday Discuss., 2015, 183, 125–145.
12 S. Ma, M. Sadakiyo, R. Luo, M. Heima, M. Yamauchi and P. J. A. Kenis, J. Power Sources, 2016, 301, 219–228.
13 H. R. M. Jhong, S. Ma and P. J. Kenis, Curr. Opin. Chem. Eng., 2013, 2, 191–199.
14 Z. Chen, P. Kang, M.-T. Zhang and T. J. Meyer, Chem. Commun. (Camb)., 2014, 50, 335–337.
15 P. Kang, Z. Chen, A. Nayak, and T. J. Meyer, Energy Environ. Sci., 2014, 07, 4007–4012.
16 K. P. Kuhl, T. Hatsukade, E. R. Cave, D. N. Abram, J. Kibsgaard, and T. F. Jaramillo, J. Am. Chem. Soc., 2014, 136, 14107–14113.
17 R. Kortlever, J. Shen, K. J. P. Schouten, F. Calle-Vallejo and M. T. M. Koper, J. Phys. Chem. Lett., 2015, 6, 4073–4082.
18 Y. Hori, Mod. Asp. Electrochem., 2008, 42, 89–189.
19 S. Zhang, P. Kang, and T. J. Meyer, J. Am. Chem. Soc., 2014, 136, 1734–1737.
20 D. Gao, H. Zhou, J. Wang, S. Miao, F. Yang, G. Wang, J. Wang, X. Bao, D. Gao, H. Zhou, J. Wang, S. Miao, F. Yang and G. Wang, J. Am. Chem. Soc., 2015, 137,4288-4291.
21 Y. Chen, C. W. Li, and M. W. Kanan, J. Am. Chem. Soc., 2012, 134, 19969–19972.
22 K. Manthiram, B. J. Beberwyck and A. P. Alivisatos, J. Am. Chem. Soc., 2014, 136, 13319–13325.
23 C. Kim, H. S. Jeon, T. Eom, M. S. Jee, H. Kim, C. M. Friend, B. K. Min, and Y. J. Hwang, J. Am. Chem. Soc., 2015, 137, 13844–13850.
24 R. Kortlever, I. Peters, S. Koper and M. T. M. Koper, ACS Catal., 2015, 5, 3916–3923.
25 X. Zhao, B. Luo, R. Long, C. Wang, and Y. Xiong, J. Mater. Chem. A Mater. energy Sustain., 2015, 3, 4134–4138.
26 Z. Xu, E. Lai, Y. Shao-Horn and K. Hamad-Schifferli, Chem. Commun., 2012, 48, 5626 -5628.
27 S. Rasul, D. H. Anjum, A. Jedidi, Y. Minenkov, L. Cavallo and K. Takanabe, Angew. Chemie Int. Ed., 2015, 54, 2146–2150.
28 P. P. Sharma, J. Wu, R. M. Yadav, M. Liu, C. J. Wright, C. S. Tiwary, B. I. Yakobson, J. Lou, P. M. Ajayan and X. D. Zhou, Angew. Chemie - Int. Ed., 2015, 54, 13701–13705.
29 H. Wang, Y. Chen, X. Hou, C. Ma, and T. Tan, Green Chem., 2016,18, 3250-3256
30 N. Sreekanth, M. A. Nazrulla, T. V. Vineesh, K. Sailaja and K. L. Phani, Chem. Commun., 2015, 51, 16061–16064.
31 S. Pal, S. Narayanaru, B. Kundu, M. Sahoo, S. Bawari, D. K. Rao, S. K. Nayak, A. J. Pal and T. N. Narayanan, J. Phys. Chem. C, 2018, 122, 23385–23392.
32 H. R. M. Jhong, C. E. Tornow, B. Smid, A. A. Gewirth, S. M. Lyth and P. J. A. Kenis, ChemSusChem, 2017, 10, 1094–1099.
33 P. Iyengar, J. Huang, G. L. De Gregorio, C. Gadiyar and R. Buonsanti, Chem. Commun. 2019, 55, 8796-8799.
34 S. Narayanaru, J. Chinnaiah, K. L. Phani, and F. Scholz, Electrochim. Acta, 2018, 264, 269-274.

35 S. Sen, D. Liu and G. T. R. Palmore, ACS Catal., 2014, 4, 3091–3095.
36 A. Murata and Y. Hori, Bull. Chem. Soc. Jpn., 1991, 64, 123–127.
37 K. P. Kuhl, E. R. Cave, D. N. Abram and T. F. Jaramillo, Energy Environ. Sci., 2012, 5, 7050–7059.
38 S. Verma, B. Kim, H. R. M. Jhong, S. Ma and P. J. A. Kenis, ChemSusChem, 2016, 9, 1972-1979.
39 J. Eppinger and K. W. Huang, ACS Energy Lett., 2017, 2, 188-195.
40 L. An and R. Chen, J. Power Sources, 2016,320,127-139.
41 S. Sankar, G. M. Anilkumar, T. Tamaki and T. Yamaguchi, ChemCatChem, 2019, 11, 4731,4737.
42 H. Kuroki, S. Miyanishi, A. Sakakibara, Y. Oshiba and T. Yamaguchi, J. Power Sources, 2019, 438, 226997.
43 A. Del Castillo, M. Alvarez-Guerra, J. Solla-Gullón, A. Sáez, V. Montiel and A. Irabien, Appl. Energy, 2015, 157, 165–173.
44 A. Álvarez, A. Bansode, A. Urakawa, A. V. Bavykina, T. A. Wezendonk, M. Makkee, J. Gascon and F. Kapteijn, Chem. Rev., 2017, 117, 9804–9838.
45 S. Lee, J. D. Ocon, Y. Il Son and J. Lee, J. Phys. Chem. C, 2015, 119, 4884–4890.
46 S. Zhao, S. Li, T. Guo, S. Zhang, J. Wang, Y. Wu and Y. Chen, Nano-Micro Lett., 2019, 11, 62.
47 X. Bai, W. Chen, C. Zhao, S. Li, Y. Song, R. Ge, W. Wei and Y. Sun, Angew. Chemie - Int. Ed., 2017, 56, 12219–12223.
48 D. H. Won, C. H. Choi, J. Chung, M. W. Chung, E. H. Kim and S. I. Woo, ChemSusChem, 2015, 8, 3092–3098.
49 Y. Fu, Y. Li, X. Zhang, Y. Liu, J. Qiao, J. Zhang and D. P. Wilkinson, Appl. Energy,2016, 175, 536-544.
50 Y. Chen and M. W. Kanan, J. Am. Chem. Soc., 2012, 134, 1986–1989.
51 M. Spichiger-Ulmann and J. Augustynski, J. Chem. Soc. Faraday Trans. 1 Phys. Chem. Condens. Phases, 1985, 81,713-716.
52 N. Sreekanth and K. L. Phani, Chem. Commun., 2014, 50, 11143–11146.
53 S. Dalton, F. Heatley, and P. M. Budd, Polymer,1999, 40, 5531-5543.
54 W. Du, K. E. MacKenzie, D. F. Milano, N. A. Deskins, D. Su and X. Teng, ACS Catal., 2012, 2, 287-297.
55 Y. Li, J. Qiao, X. Zhang, T. Lei, A. Girma, Y. Liu and J. Zhang, ChemElectroChem, 2016, 3, 1618–1628.
56 B. Jiang, X. G. Zhang, K. Jiang, D. Y. Wu and W. Bin Cai, J. Am. Chem. Soc., 2018, 140, 2880-2889.
57 S. Sankar, G. M. Anilkumar, T. Tamaki and T. Yamaguchi, ACS Appl. Energy Mater., 2018, 1, 4140–4149.
58 Z. Li, Y. Chen, G. Fu, Y. Chen, D. Sun, J. M. Lee, and Y. Tang, Nanoscale, 2019, 11, 2974–2980.
59 X. Min and M. W. Kanan, J. Am. Chem. Soc., 2015, 137, 4701–4708.
60 R. Kortlever, C. Balemans, Y. Kwon and M. T. M. Koper, Catal. Today, 2015, 244, 58–62.
61 S. Chatterjee, C. Griego, J. L. Hart, Y. Li, M. L. Taheri, J. Keith, and J. D. Snyder, ACS Catal., 2019, 9, 5290–5301.
62 W. Zhang, Q. Qin, L. Dai, R. Qin, X. Zhao, X. Chen, D. Ou, J. Chen, T. Chuong, B.Wu. Angew. Chemie - Int. Ed. 2018, 57, 9475–9479.
63 J. T. Feaster, C.Shi, E. R.Cave, T.Hatsukade, D. N. Abram, K. P. Kuhl, C. Hahn, J. K. Nørskov, T. F. Jaramillo, ACS Catal. 2017, 7, 4822–4827.

Table of Contents

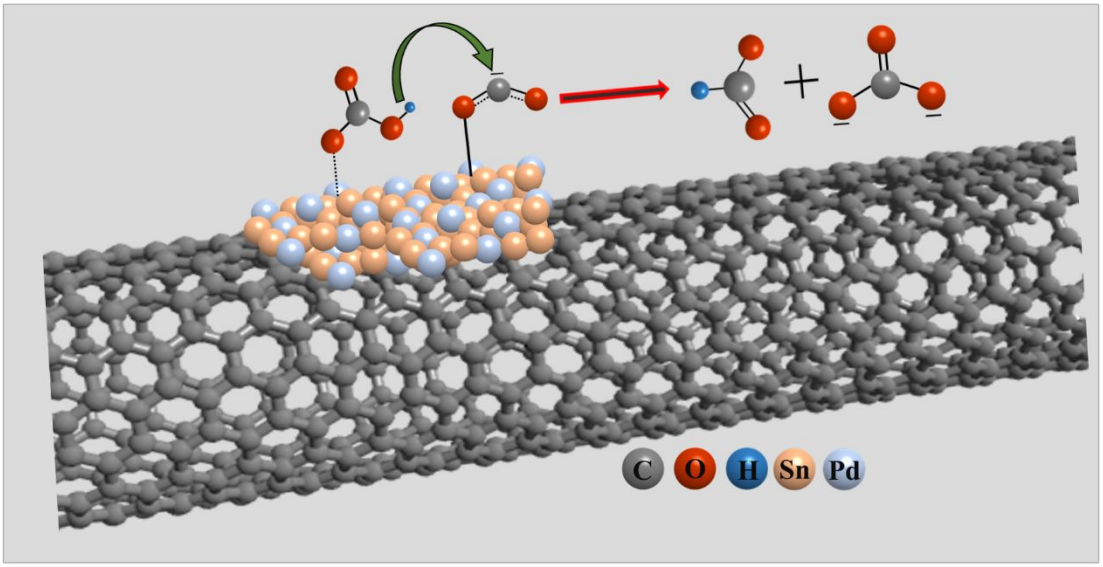

Electrochemical reduction of CO_2 to formate on SnPd–NCF. The adsorbed bicarbonate ion promotes the protonation of $CO_2^{\bullet-}$ to HCO_2^-.